JCI insight

Organelle communication maintains mitochondrial and endosomal homeostasis during podocyte lipotoxicity

Sho Hasegawa, … , Takashi Kadowaki, Reiko Inagi

JCI Insight. 2024. https://doi.org/10.1172/jci.insight.182534.

Research In-Press Preview Nephrology

Graphical abstract

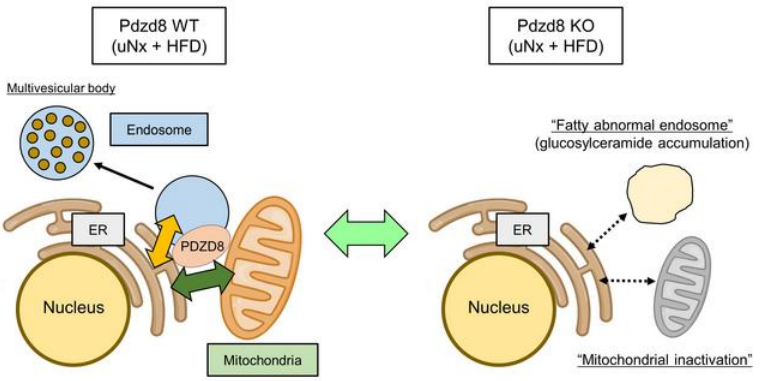

Organelle communication maintains mitochondrial and endosomal homeostasis during podocyte lipotoxicity

Sho Hasegawa[1, 2], Masaomi Nangaku[2], Yuto Takenaka[1, 2], Chigusa Kitayama[1, 2], Qi Li[1, 2], Madina Saipidin[1, 2], Yu Ah Hong[1, 2], Jin Shang[1, 2], Yusuke Hirabayashi[3], Naoto Kubota[4, 5], Takashi Kadowaki[5, 6, 7], and Reiko Inagi[1*]

1. Division of Chronic Kidney Disease Pathophysiology, Graduate School of Medicine, The University of Tokyo, Tokyo, Japan.

2. Division of Nephrology and Endocrinology, Graduate School of Medicine, The University of Tokyo, Tokyo, Japan.

3. Department of Chemistry and Biotechnology, School of Engineering, The University of Tokyo, Tokyo, Japan.

4. Department of Metabolic Medicine, Faculty of Life Science, Kumamoto University, Kumamoto, Japan.

5. Department of Diabetes and Metabolic Diseases, Graduate School of Medicine, The University of Tokyo, Tokyo, Japan.

6. Department of Prevention of Diabetes and Lifestyle-Related Diseases, Graduate School of Medicine, The University of Tokyo, Tokyo, Japan.

7. Toranomon Hospital, Tokyo, Japan.

***Corresponding author**: Reiko Inagi, PhD.

Graduate School of Medicine, The University of Tokyo, 7-3-1 Hongo, Bunkyo-ku, Tokyo 113-8655, Japan.

E-mail: inagi-r@m.u-tokyo.ac.jp

Tel: +81-3-3815-5411 (ext. 36703)

Conflict-of-interest statement

Division of CKD pathophysiology, Graduate School of Medicine, the University of Tokyo is financially supported by Kyowa Kirin Co., Ltd.

Abstract

Organelle stress exacerbates podocyte injury, contributing to perturbed lipid metabolism. Simultaneous organelle stresses occur in kidney tissues; therefore, a thorough analysis of organelle communication is crucial for understanding the progression of kidney diseases. Although organelles closely interact with one another at membrane contact sites, limited studies have explored their involvement in kidney homeostasis. The endoplasmic reticulum (ER) protein, PDZ domain-containing 8 (PDZD8), is implicated in multiple organelle tethering processes and cellular lipid homeostasis. In this study, we aimed to elucidate the role of organelle communication in podocyte injury using podocyte-specific *Pdzd8*-knockout mice. Our findings demonstrated that *Pdzd8* deletion exacerbated podocyte injury in an accelerated obesity-related kidney disease model. Proteomic analysis of isolated glomeruli revealed that *Pdzd8* deletion exacerbated mitochondrial and endosomal dysfunction during podocyte lipotoxicity. Additionally, electron microscopy revealed the accumulation of “fatty abnormal endosomes” in *Pdzd8*-deficient podocytes during obesity-related kidney diseases. Lipidomic analysis indicated that glucosylceramide accumulated in *Pdzd8*-deficient podocytes, owing to accelerated production and

decelerated degradation. Thus, the organelle-tethering factor, PDZD8, plays a crucial role in maintaining mitochondrial and endosomal homeostasis during podocyte lipotoxicity. Collectively, our findings highlight the importance of organelle communication at the three-way junction among the ER, mitochondria, and endosomes in preserving podocyte homeostasis.

Key words: endosome, lipotoxicity, mitochondria, obesity-related kidney disease, organelle contact sites

Introduction

Organelles are confined functional subunits within the cell. Various essential biochemical reactions for maintaining cellular homeostasis, including energy metabolism, protein quality control, and degradation, occur within organelles. The cytoplasmic separation of organelles enables each to have a distinct role and perform complex cellular functions (1).

Organelle stress is a major exacerbating factor in podocyte injury, leading to dysregulated lipid metabolism. For example, mitochondrial dysregulation compromises mitochondrial lipid utilization, ultimately resulting in lipid accumulation and lipotoxicity (2). Additionally, in an obesity-related kidney disease model, podocyte-specific autophagy-deficient mice exhibit more severe albuminuria and podocyte damage than that in their littermate controls (3).

Recent advances in imaging techniques have revealed close interactions between organelles at membrane contact sites (MCS). For example, mitochondria and the endoplasmic reticulum (ER) form mitochondria-ER contact sites (MERCS), serving as a unique subcellular platform for metabolite exchange, such as Ca^{2+} and glycerophospholipids (4, 5). Furthermore, endosome maturation, involving the conversion of early endosomes to late endosomes for

subsequent fusion with lysosomes, occurs at contact sites between endosomes and the ER through lipid transfer in neuronal cells (6, 7). Thus, organelle communication via MCS is crucial for cellular homeostasis. However, few studies have explored the involvement of MCS in kidney homeostasis, partly owing to technical challenges in analyzing in vivo organelle communication.

The ER protein PDZ domain-containing 8 (PDZD8) plays a pivotal role in multiple organelle tethering and cellular lipid homeostasis. PDZD8 is essential for MERCS formation, mediating Ca^{2+} transfer from the ER to mitochondria in various cell types (4, 8, 9). Additionally, PDZD8 is located at ER-endosome contact sites, promoting endosome maturation through lipid transfer (7, 8, 10, 11).

To address the gaps in the literature, in this study, we aimed to elucidate the involvement of organelle communication and perturbed lipid homeostasis in podocyte injury, with a specific focus on the function of PDZD8 as a multiple-organelle tethering factor.

Results

Pdzd8 deletion induces podocyte endosomal malformation in an obesity-related kidney disease

Podocyte-specific *Pdzd8* conditional knockout mice (podocin-Cre: *Pdzd8* flox/flox, cKO) and littermate wild-type controls (*Pdzd8* flox/flox, WT) were generated. Genotype analysis was conducted using tail PCR (Supplementary Figure S1A, B), and *Pdzd8* deletions in podocytes were validated using quantitative real-time PCR of the isolated glomeruli (Supplementary Figure S1C). The mice were divided into two groups and fed either a normal diet (ND) or a high-fat diet (HFD) for 12 weeks (Figure 1A).

Urinary albumin levels, a marker of podocyte injury, were higher in the HFD group than that in the ND group. However, urinary albumin levels did not significantly differ between the HFD-WT and HFD-cKO groups (Figure 1B). Background data, such as body weight, plasma cholesterol, plasma triglyceride, blood urea nitrogen (BUN), and plasma creatinine levels, did not significantly differ between the HFD-WT and HFD-cKO groups (Supplementary Figure S2A-E). Although optical microscope imaging using PAS staining did not reveal significant differences between HFD-WT and HFD-cKO (Supplementary Figure

S2F), we observed the presence of abnormal endosomes in HFD-cKO groups using electron microscopy (Figure 1C, D, yellow arrow), resembling “abnormal large vacuoles” observed in *Pdzd8*-deleted Hela cells and neurons in the previous studies (7).

***Pdzd8* deletion affects mitochondrial and endosomal homeostasis during podocyte lipotoxicity**

To elucidate the mechanism underlying the emergence of abnormal endosomes in the podocytes of HFD-cKO mice, we isolated glomeruli and performed a comprehensive proteomic analysis (Supplementary Table S1, jPOST repository accession number JPST002955). The ND-WT, ND-cKO, HFD-WT, and HFD-cKO groups were distinctly distributed in principal component analysis (PCA) plots, indicating differences in proteomic profiles (Figure 2A). Notably, “mitochondrial gene expression” and “endosome organization” were enriched by the gene ontology (GO) analysis of differentially expressed 173 proteins between the HFD-WT and HFD-cKO groups (Figure 2B, C, Supplementary Table S2). When examining individual proteins, PDZD8 levels were reduced in the cKO group compared with the WT group (Figure 2D). The quantity of proteins related to

mitochondrial FAO, including carnitine palmitoyltransferase 1b (CPT1B) and acyl-CoA synthetase short-chain family member 1 (ACSS1), was lower in HFD-cKO mice than that in HFD-WT mice (Figure 2E, F). Additionally, the level of hook microtubule tethering protein 1 (HOOK1), which is related to endosome organization, was lower in HFD-cKO mice than that in HFD-WT mice (Figure 2G). Collectively, a comprehensive proteomic analysis of isolated glomeruli revealed that *Pdzd8* deletion affects mitochondrial and endosomal homeostasis during podocyte lipotoxicity.

***Pdzd8* deletion exacerbates podocyte injury in an accelerated obesity-related kidney disease model**

To elucidate the impact of *Pdzd8* deletion-induced mitochondrial and endosomal abnormalities on podocyte injury, we established an accelerated obesity-related kidney disease model. WT and cKO mice were subjected to uninephrectomy (uNx) and exposed to HFD for 12 weeks (Figure 3A). Notably, significantly elevated urinary albumin levels, a marker of podocyte injury, were observed in uNx-HFD-cKO mice compared with that in uNx-HFD-WT mice (Figure 3B). Background data, including body weight, plasma cholesterol, plasma triglyceride,

BUN, and plasma creatinine levels, did not significantly differ between uNx-HFD-WT and uNx-HFD-cKO groups (Supplementary Figure S3A-E).

Optical microscopy imaging with PAS staining did not reveal a significant difference between uNx-HFD-WT and uNx-HFD-cKO mice (Supplementary Figure S3F). However, the number of Wilms tumor 1 (WT1) positive cells per glomerulus was significantly reduced in uNx-HFD-cKO mice, compared with uNx-HFD-WT mice (Supplementary Figure S4). Moreover, electron microscopy imaging indicated numerous abnormal endosomes in the podocytes of uNx-HFD-cKO mice (Figure 3C, D, orange arrows), labeled as “fatty endosomes," suggesting a more advanced dysfunctional stage than those observed in HFD-cKO mice (Figure 1D). These endosomes were speculated to contain excessive lipids, prompting further investigation into their emergence mechanism.

Pdzd8 knockdown inhibits mitochondrial and FAO activity in podocytes

To corroborate the in vivo proteomic phenotype of mitochondrial abnormalities associated with PDZD8, we performed cell culture experiments using mouse podocytes (HSMP). Exposure of differentiated mouse podocytes to palmitic acid (PA) upregulated the mRNA expression of key FAO molecules, *Cpt1a* and *Cpt2*.

Pdzd8 knockdown using siRNA significantly inhibited the expression of these molecules at both early (3 h) and late (18 h) stages (Figure 4A). Proteomic analysis revealed a significant reduction in CPT1A protein levels after PA exposure (18 h) following *Pdzd8* knockdown (Supplementary Figure S5A, jPOST repository accession number JPST002956). Additionally, *Pdzd8* knockdown decreased the expression of peroxisome proliferator-activated receptor-gamma coactivator 1-alpha (*Pgc1a*), a mitochondrial biosynthesis factor (Figure 4A). These phenotypes were consistent across multiple siRNA sequences, including *Pdzd8* siRNA (#2) (Supplementary Figure S5B).

We further performed a Mito Stress test with PA and etomoxir (CPT1 inhibitor) to assess mitochondrial oxygen consumption rate (OCR) and FAO activity (Figure 4B). *Pdzd8* knockdown significantly reduced basal and maximal OCR in both the absence and presence of etomoxir (Figure 4C). Moreover, *Pdzd8* knockdown inhibited FAO activity in both basal and maximal mitochondrial states (Figure 4D). Collectively, our findings suggest that *Pdzd8* knockdown inhibits mitochondrial activity, including that of FAO, in cultured podocyte cell lines.

We also performed the flow cytometry analysis using Annexin V and propidium iodide (PI) to assess the rate of podocyte apoptosis. As a result, *Pdzd8*

knockdown increased the apoptosis of PA-treated podocytes (Supplementary Figure S6). These data are consistent with the decrease in WT1-positive cells per glomerulus in uNx-HFD-cKO mice (Supplementary Figure S4).

Pdzd8 knockdown results in a reduction of MERCS in podocytes

To explore interactions between the ER and mitochondria, we performed PLA, which helps assess the proximity between proteins at the MERCS, utilizing VDAC and IP3R proteins representing the outer mitochondrial and ER membranes, respectively. The assay revealed a significant decrease in ER-mitochondrial interactions in *Pdzd8* knockdown podocytes compared with that in controls (Figure 5, Supplementary Figure S7). This reduction in ER-mitochondrial interactions induced by *Pdzd8* knockdown may contribute to mitochondrial inactivation.

Lipids from cellular membranes accumulate in "fatty endosomes" in Pdzd8 knockdown podocytes following PA treatment

To explore the origin of "fatty endosomes," we performed a FA pulse-chase assay using FA tail-tagged phosphatidylcholine fluorescence (FL HPC) (Figure 6A) (12). Initial labeling of cultured podocytes with FL HPC, which integrates into various cellular membranes, revealed significantly higher FL HPC and LysoTracker Red co-localization in PA-treated podocytes compared with that in BSA-treated podocytes (Figure 6B), suggesting that PA treatment mobilized lipids from cellular membranes to endosomes. Notably, enlarged endosomes co-localized with FL HPC were observed in PA-treated *Pdzd8* knockdown podocytes (Figure 6B, orange arrowhead), resembling “fatty endosomes” observed in the podocytes of uNx-HFD-cKO mice (Figure 3C, D). Moreover, at a later stage (PA treatment for 18 h), RAB7-labeled endosomes significantly accumulated in *Pdzd8* knockdown podocytes compared with that in the negative control siRNA-treated group (Supplementary Figure S8, 9). Thus, lipids from cellular membranes may accumulate in “fatty endosomes” in *Pdzd8* knockdown podocytes after PA treatment.

Pdzd8 knockdown induces glucosylceramide accumulation in podocytes

To identify the lipid types accumulating in "fatty endosomes," we performed non-targeted lipidome analysis on cultured podocytes (Figure 7A, Supplementary Table S3). While the lipid profiles differed between the BSA and PA treatment groups, no significant differences were observed in lipid profiles between control and *Pdzd8* knockdown podocytes (Figure 7B). However, examination of upregulated lipids attributable to *Pdzd8* knockdown (Figure 7C) revealed enrichment in glucosylceramide (Hex1Cer) (Figure 7D).

As glucosylceramide production involves regulation by glucosylceramide synthase (UDP-glucose ceramide glucosyltransferase: UGCG), and glucosylceramide degradation involves regulation by glucosylceramidase beta 1 (GBA1) and glucosylceramidase beta 2 (GBA2), their expressions were investigated. Quantitative real-time PCR showed that *Pdzd8* knockdown increased *Ugcg* (synthesis) expression and decreased *Gba1* (degradation in endosomes) expression (Figure 7E). In contrast, *Gba2* (degradation at the ER) expression did not differ between control and *Pdzd8* knockdown podocytes (Figure 7E). Consistently, in vivo, *Pdzd8* knockout tended to increase UGCG expression and decreased GBA2 expression in the isolated glomeruli of a HFD model (Supplementary Figure S10). Thus, *Pdzd8* knockdown induces

glucosylceramide accumulation in podocytes by activating the synthesis and reducing the degradation in endosomes, which might at least partly contribute to the emergence of “fatty endosomes” in *Pdzd8*-deleted podocytes.

We also performed the *Gba1* knockdown experiments to examine the effects of glucosylceramide accumulation on podocyte conditions. The flow cytometry analysis using Annexin V and PI showed that *Gba1* knockdown increased the apoptosis of podocytes after 18h PA exposure (Supplementary Figure S11). Moreover, *Gba1* knockdown reduced the expression of *Pgc1a*, *Cpt1a*, and *Cpt2* in podocytes (Supplementary Figure S11), suggesting that glucosylceramide accumulation inhibited mitochondrial and FAO activity.

Discussion

In this study, we demonstrated that the organelle-tethering factor, PDZD8, plays a crucial role in maintaining mitochondrial and endosomal homeostasis during podocyte lipotoxicity (Figure 8). *Pdzd8* deficiency inhibits mitochondrial activity, including FAO, leading to the accumulation of “fatty endosomes.” This accumulation is partly attributed to the acceleration of glucosylceramide production and the deceleration of its degradation during obesity-related kidney disease. These findings highlight the significant contribution of three-way organelle communication among the ER, mitochondria, and endosomes to podocyte homeostasis.

During the progression of diabetic kidney disease (DKD), organelle stressors, such as excessive ATP production (mitochondrial stress) and maladaptive unfolded protein response (UPR; ER stress), occur simultaneously in kidney tissues (13, 14). Furthermore, the reduced intraflagellar transport protein 88 (IFT88) expression in cisplatin-induced acute kidney injury (AKI) shortens primary cilia and leads to mitochondrial dysfunction (15). These findings emphasize the importance of detailed analysis of organelle communication in understanding organelle stress in kidney disease.

Extensive research on MERCS in various diseases suggests that their disruption contributes to insulin resistance in the liver (16) and muscles (17). Overexpression of mitofusin-2 (18) and glucose-regulated protein 75 (19), which are pivotal components of MERCS, in hepatocytes effectively prevents palmitate-induced insulin signaling deficiency. The role of MERCS extends to kidney disease progression, where its disruption occurs at the early stages of gentamicin-induced AKI. This disruption precedes downstream activation of the UPR and subsequent cell death (20). Furthermore, increased expression of the ER-resident protein reticulon-1A contributes to tubular injury, tubulointerstitial fibrosis, and a decline in kidney function during the early stages of DKD by regulating ER-mitochondria contacts (21). Additionally, urine metabolome analysis has identified lysophosphatidylcholine (LPC) accumulation as a negative prognostic factor for DKD. The accumulation of LPC in proximal tubular cells decreases MERCS and leads to cell death (22).

Our study introduces a novel perspective by emphasizing the significance of the three-way organelle-tethering factor and elucidates that the communication among the ER, mitochondria, and endosomes significantly contributes to maintaining podocyte homeostasis. However, the impact of *Pdzd8* deletion on

albuminuria was less pronounced than anticipated despite the evident organelle dysfunctions observed, including the presence of "fatty endosomes" in *Pdzd8*-deleted podocytes.

There may be three reasons for this observed discrepancy. First, glomerular filtration is a passive process and does not require a substantial amount of ATP, rendering podocytes less sensitive to mitochondrial dysfunction (23). Second, in terms of protein degradation, the ubiquitin-proteasome system might play a more pivotal role than the autophagy-endosome system in maintaining intracellular homeostasis in podocytes (24). While the specific deficiency of autophagy in podocytes exhibited no discernible histological phenotype in young mice (25, 26), the impairment of the podocyte-specific proteasome led to apoptosis and the development of glomerulosclerosis at a young age (24). Hence, the ubiquitin-proteasome system might compensate for the endosomal deficiency induced by *Pdzd8* deletion. Third, *Pdzd8* deficiency results in the accumulation of glucosylceramide. Cardiolipin accumulation is reportedly implicated in podocyte lipotoxicity (27). However, our lipidome analysis indicated that *Pdzd8* deletion did not induce cardiolipin accumulation but rather led to the accumulation of glucosylceramide in podocytes, which is similar to that

in Gaucher disease. Gaucher disease is a rare, inherited metabolic disorder in which deficiency of GBA1 results in glucosylceramide accumulation throughout the body, particularly in the bone marrow, spleen, and liver (28). In contrast to Fabry disease, patients with Gaucher disease typically do not experience rapid progression of kidney disease, suggesting that glucosylceramide accumulation might not significantly impact podocyte homeostasis.

The detailed mechanism underlying the fact that *Pdzd8* deletion increases the expression of *Ugcg* and decreases the expression of *Gba1* in podocytes remains elusive. However, the previous study showed that UGCG directly interacted with reticulon-1 in MERCS (29). The increased expression of *Ugcg* in *Pdzd8* knockdown podocytes might be attributed to the disruption of MERCS. As GBA1 is expressed in endosomes, the decreased expression of *Gba1* in *Pdzd8* knockdown podocytes might be induced by endosomal dysfunction.

This study has the following limitations: First, our study focused on PDZD8 functions rather than organelle tethering. We acknowledge that PDZD8 may have additional roles beyond being a three-way organelle-tethering factor among the ER, mitochondria, and endosomes. Thus, we cannot conclude

whether the phenotypes of podocyte-specific *Pdzd8* deletion are primarily attributed to the disruption of organelle communications. However, the knockdown of Inositol 1,4,5-trisphosphate receptor type 3 (*Itpr3*), another MERCS factor, also induced mitochondrial inactivation in podocytes (Supplementary Figure S12). Thus, the role of PDZD8 in mitochondrial function might be associated with the disruption of MERCS. Second, we performed whole-cellular lipidomics to identify the origin of “fatty endosomes.” Although isolating these endosomes and performing lipidomic analysis is imperative to comprehensively investigate the role of these “fatty endosomes,” maintaining consistent purity in the organelles isolated from podocytes with different injury statuses is technically complex. Thus, we cannot conclude whether glucosylceramide was specifically increased within the “fatty endosomes” or in the other cellular fractions.

Nevertheless, our findings demonstrate that PDZD8 serves as a critical organelle-tethering factor, maintaining mitochondrial and endosomal homeostasis during podocyte lipotoxicity (Figure 8). Its deficiency inhibits mitochondrial activity, including FAO, induces "fatty endosome" accumulation by accelerating the production and decelerating the degradation of

glucosylceramide, and contributes to obesity-related kidney disease. Further research on additional organelle-tethering factors is required to comprehensively elucidate the role of organelle communication in podocyte homeostasis.

Methods

Sex as a biological variable

Our study examined male mice because male animals exhibited less variability in phenotype.

Animal experiments

Male C57BL/6 mice (9–10 weeks of age, 20-25 g) were used for all experiments. Podocyte-specific *Pdzd8* cKO mice were generated by crossbreeding Podocin-Cre (30) and *Pdzd8* flox mice (31). Genotyping was performed by tail PCR using published primers (Supplementary Figure S1A, B, Supplementary Table S4). HFD-60 (Oriental Yeast Co., Ltd., Japan) was used as the high fat diet (Calorie ratio of fatty acids is 62.2%). CE-2 (Clea Japan, inc.) was used as the normal diet (Calorie ratio of fatty acids is 4.77%).

Uninephrectomy

Mice were anesthetized by the intraperitoneal administration of medetomidine 0.3 mg/kg, butorphanol 5 mg/kg, and midazolam 4 mg/kg. Left-side unilateral nephrectomy was performed, and the wound was sutured.

Kidney function and histological analyses

Plasma of heparinized blood was separated by centrifugation at 7,000 × g for 5 min at room temperature. Plasma cholesterol, plasma triglyceride, BUN and plasma creatinine levels were measured by SRL Inc. (Osaka, Japan). Urinary albumin and creatinine levels were measured by Oriental Yeast Co., Ltd. (Nagahama, Japan). For histological analyses, the kidney tissues were fixed in Mildform 10N (133-10311, Wako, Japan), dehydrated, and embedded in paraffin. The paraffin-embedded samples were cut into 3-μm-thick sections, stained with periodic acid–Schiff (PAS) reagent. As for the WT1 staining, antigen retrieval was carried out using microwave irradiation (500 W, 5 min, twice). Endogenous peroxidase was inactivated by treatment with 3% hydrogen peroxide. The kidney slices were incubated with the anti-WT1 antibody (1:300 dilution, ab89901, abcam, UK) at 4 °C overnight. After incubated with the HRP-conjugated secondary antibody (Histo-fine simple stain mouse MAX-PO, 414341, Nichirei,

Japan), diaminobenzidine (DAB) reaction was performed using ImmPACT DAB peroxidase substrate (SK-4105, Vector Laboratories, US) according to the manufacturer's instructions.

Electron microscopy

The kidney tissues were fixed with 2% paraformaldehyde and 2.5% glutaraldehyde in 0.1M phosphate buffer (pH 7.4). The samples were postfixed with 1% osmium tetroxide, dehydrated, and embedded in Epok 812. Ultrathin sections were stained with uranyl acetate and lead citrate. The samples were observed using an electron microscopy JEM-1400 Flush (JEOL Ltd., Japan).

Glomerular isolation

Mouse glomeruli were isolated using a previously described method with some modifications (30). Briefly, we perfused magnetic Dynabeads M-450 (DB14013, Invitrogen) through the left ventricle of the heart. After removal, kidneys were minced into small pieces, digested by collagenase A (2 mg/mL, 10103586001, Roche, Basel, Switzerland) and DNase I (200 units/mL, 04716728001, Roche),

and filtered through a 100 μm cell strainer with sterile PBS. After washing several times, the glomeruli were collected using a magnet. The purity of glomeruli was confirmed to be 95% in each sample by phase-contrast microscopy.

Proteomics

Glomerular and cellular proteomics was performed and analyzed by Kazusa DNA Research Institute (Chiba, Japan) (32-34). The PCA and the comparison between groups were performed using Perseus (https://maxquant.net/perseus/) (35). PCA decomposes the original data into a set of new variables that are linear combinations of the original variables. The component 1 is the line that best accounts for the shape of the point swarm. It represents the maximum variance direction in the data. The component 2 is oriented such that it reflects the second largest source of variation in the data while being orthogonal to the component 1. The definition of differentially expressed proteins was |log2FoldChange| > 1 and P-value < 0.05. The gene ontology (GO) analysis of differentially expressed proteins was performed using Metascape (https://metascape.org/) (36).

Lipidomics

Cellular lipidomics was conducted according to Lipidome lab Non-targeted Lipidome Scan package (Lipidome lab, Akita, Japan), using liquid chromatograph orbitrap mass spectrometry based on the methods described previously (37, 38). Hierarchical cluster analysis (HCA) and PCA were performed by Human Metabolome Technologies, Inc. (HMT, Tsuruoka, Japan), using HMT's proprietary MATLAB and R programs, respectively (39).

RNA isolation and quantitative real-time PCR

Total mRNA was isolated from cultured cells or mouse tissue samples using the RNeasy Mini Kit (74106, Qiagen, Hilden, Germany), and 50 ng mRNA in a total reaction volume of 20 μL was reverse-transcribed using PrimeScript RT Master Mix (Takara Bio, Japan) according to the manufacturers' protocols.

The complementary DNA (cDNA) generated was used as the template for quantitative real-time PCR that was performed with Fast SYBR Green Master Mix (Thermo Fisher Scientific, Waltham, MA) on a StepOnePlus real-time PCR system (Thermo Fisher Scientific). β-actin was used as the reference gene. Relative gene expression levels were calculated from delta cycle threshold

values (CT; $2^{-\Delta\Delta Ct}$) (40). The primer sequences used in this study are listed in Table 1.

Cell culture

Conditionally immortalized heat sensitive mouse podocytes (HSMP) were generated and characterized as described previously (30, 41, 42). The cells were grown in RPMI-1640 media with HEPES (189-02145, Wako, Japan) containing 10% FBS (Thermo Fisher Scientific, Waltham, MA), sodium pyruvate (1 mmol/L; Wako, Japan). To passage cells, podocytes were grown under permissive conditions (33°C in the presence of IFN-g; 50 units/mL). For podocytes to acquire differentiation and quiescence resembling the in vivo phenotype, cells were grown under restrictive conditions at 37°C in 95% air/5% CO2 without IFN-g for 14 days. All experiments were performed using podocytes under growth-restricted, differentiated conditions.

RNA interference

Gene expressions were suppressed using Silencer Select Pre-designed siRNAs (Thermo Fisher Scientific) against mouse *Pdzd8* (s98833 as #1 and s98834 as #2), mouse *Gba1* (s66492), and mouse *Itpr3* (s68521). A supplier-matched control Silencer Select Negative Control No. 1 siRNA (4390843, Thermo Fisher Scientific) was used as the negative control. The siRNAs (5 nM) were introduced into mouse podocyte cells using Opti-MEM I Reduced Serum Medium (31985070, Thermo Fisher Scientific) and Lipofectamine RNAiMAX transfection reagent (13778150, Thermo Fisher Scientific) according to the manufacturer's instructions.

Analysis of mitochondrial function and fatty acid oxidation (FAO)

The intracellular bioenergetic profiles of cells were determined with an XFe96 Seahorse extracellular flux analyzer (Agilent Technologies, Santa Clara, CA), using the Mito Stress Test Kit (103015–100, Agilent Technologies) according to the manufacturer's protocol (15). The concentrations of glucose, pyruvate, and glutamine in the assay media were 10 mM, 1 mM, and 2 mM, respectively. The concentrations of oligomycin, carbonylcyanide-4-trifluoromethoxyphenylhydrazone (FCCP), and antimycin A/rotenone during Mito

Stress tests were 2 μM, 0.5 μM, and 1 μM, respectively. To measure FAO activity, palmitate (PA)-conjugated BSA (102720–100, Agilent Technologies) and etomoxir (40 μM), an inhibitor of CPT1 were added to the medium before the assay. FAO activity was defined as the etomoxir-induced decrease in basal and maximal OCR.

Flow cytometry analysis

Apoptosis assay was performed using Annexin V-FITC Apoptosis Detection Kit (15342-54, Nacalai, Japan). The flow cytometry analysis was conducted using CytoFLEX System (Beckman Coulter, US).

Immunofluorescence staining

For immunofluorescence staining, the cells were seeded at 8×10^4 cells/well in 35 mm glass-base dish coated with collagen (D11134H, Iwaki, Japan). After aspiration of the culture medium, the cells were washed with phosphate buffered saline (PBS) and then fixed with 4% paraformaldehyde solution (163–20145, Wako, Japan) for 10 min. The fixed cells were washed three times with PBS and

were then permeabilized with 0.3% Triton X-100-containing PBS for 10 min. The cells were blocked with 1% bovine serum albumin (BSA) in PBS for 30 min. After incubation with primary antibodies for 1 h, the cells were washed three times with PBS and then incubated with secondary antibodies for an additional hour. Thereafter, the cells were once again washed three times with PBS. Cytoskeletons were stained with Alexa Fluor 488 phalloidin (A12379, Thermo Fisher Scientific) and nuclei were stained with Hoechst 33342 (B2261, Sigma-Aldrich). All procedures were performed at room temperature. The samples were observed using a BZ-X700 fluorescence microscope (KEYENCE, Osaka, Japan). Image analysis was performed by ImageJ software (43).

The following primary antibody was used for staining: rabbit monoclonal anti-RAB7 [EPR7589] (1:500 dilution, ab137029, Abcam, UK). The following secondary antibody was used: goat anti-rabbit IgG (H+L) cross-adsorbed secondary antibody, Texas Red (1:1000 dilution, T-2767, Thermo Fisher Scientific).

Proximity Ligation Assay (PLA)

For proximity ligation assay (PLA), Duolink In Situ Red Starter Kit Mouse/Rabbit (DUO92101, Sigma-Aldrich St. Louis, USA) was used (44, 45). The cells were seeded at 8 × 10^4 cells/well in 35 mm glass-base dish coated with collagen (D11134H, Iwaki, Japan). After aspiration of the culture medium, the cells were washed with PBS and then fixed with 4% paraformaldehyde solution (163–20145, Wako, Japan) for 10 min. The fixed cells were washed three times with PBS and were then permeabilized with 0.3% Triton X-100-containing PBS for 30 min. Blocking was performed using Duolink blocking solution for 1 h at 37°C. Incubations with primary antibodies (VDAC1 and IP_3R-1, 1:100 in Duolink Antibody diluent) were performed overnight at 4°C in a humidity chamber. Then, the cells were rinsed with Wash Buffer A. Next, PLUS and MINUS secondary PLA probes, both rabbit and mouse immunoglobulins diluted in Duolink Antibody diluent, were added for 1 h at 37°C. The incubation was followed by 5 min washes in two changes of Wash Buffer A. After this, the dishes were incubated with the Duolink ligation mix for 30 min at 37°C and thereafter washed with two changes of Wash Buffer A for 5 min each. The Duolink amplification mix was then applied to the dishes for 100 min at 37°C. Subsequently, the dishes were washed twice for 10 min each time with Wash Buffer B. Cytoskeletons were stained with Alexa

Fluor 488 phalloidin (A12379, Thermo Fisher Scientific) and nuclei were stained with Hoechst 33342 (B2261, Sigma-Aldrich). The samples were observed using a BZ-X700 fluorescence microscope (KEYENCE, Osaka, Japan). Image analysis was performed by ImageJ software (43).

The following primary antibodies were used for staining: rabbit polyclonal anti-VDAC1 antibody (1:100 dilution, 55259-1-AP, Proteintech, Rosemont, USA) and mouse monoclonal IP_3R-1 (E-8) antibody (1:100 dilution, sc-271197, Santa Cruz, Dallas, USA).

Fluorescence Fatty Acid (FA) Pulse-Chase Assay

Fluorescence FA pulse-chase assay was performed as previously described, with slight modification (12). Mouse podocytes were incubated with the culture media containing 2 mM b-BODIPY FL C12-HPC (FL HPC) (Invitrogen) for 16 hours. Cells were then washed three times with the normal culture media, incubated for 1 hour to allow the fluorescent lipids to incorporate into cellular membranes, and then chased for the indicated times under BSA or PA-BSA (0.1mM) treatment. FL-HPC–loaded and chased cells were stained with 50 nM LysoTracker Red DND-99 for 30 minutes at 37°C and their nuclei were stained with Hoechst 33342

(B2261, Sigma-Aldrich). The samples were observed using a BZ-X700 fluorescence microscope (KEYENCE, Osaka, Japan).

Statistical analysis

The data are expressed as mean ± standard deviation (SD). Student's *t*-test (unpaired two-tail) was used for the comparisons between two subgroups. For multiplex comparisons, a two-way analysis of variance (ANOVA) followed by a *post hoc* Tukey's multiple comparisons test was applied. *P*-value < 0.05 was considered statistically significant. All statistical analyses were performed using the Prism 10 software (GraphPad Software, Inc., San Diego, CA).

Study approval

All animal experiments were approved by the University of Tokyo Institutional Review Board (approval number: P20-098 and H22-184). All animal procedures were performed according to the National Institutes of Health (NIH, USA) guidelines (Guide for the Care and Use of the Laboratory Animals).

Data availability

The Glomerular and cellular proteomics data supporting the findings of this study are openly available in repository jPOST (https://repository.jpostdb.org/) (46) under accession number JPST002955 and JPST002956, respectively. Values for all data points in graphs are reported in the Supporting Data Values file.

Authors' contributions

SH, MN, and RI designed the study. SH performed most of the experiments. YH provided technical advice. YT, CK, QL, MS, YAH, and JS provided technical support for the experiments. NK and TK provided conceptual advice. SH wrote the original manuscript. All authors revised the manuscript and approved the final version.

Acknowledgements

We are grateful to Dr. Osamu Ohara (Kazusa DNA Research Institute) for valuable discussions. We also thank Ms. Ikumi Okuaki, Ms. Keiko Miyamoto and Ms. Yoriko Akuzawa (The University of Tokyo) for their technical support. The illustrations of mice in Figures were obtained from TogoTV (© 2016 DBCLS TogoTV).

This work was supported by the Japan Society for the Promotion of Science (JSPS) Grant-in-Aid for Early-Career Scientists (21K16159 to SH), the JSPS Grant-in-Aid for Scientific Research B (21H02824 to RI and 23H02924 to MN), Kyowa Kirin (to RI), Grants from MSD Life Science Foundation (to SH), The Cell Science Research Foundation (to SH), Takeda Science Foundation (to SH),

The Ichiro Kanehara Foundation for the Promotion of Medical Sciences and Medical Care (to SH), Ono Medical Research Foundation (to SH), Ishibashi-Yukiko Kinen-Kikin (to SH), Japan Arteriosclerosis Prevention Fund (to SH), Mochida Memorial Foundation for Medical and Pharmaceutical Research (to SH), The Japan Kidney Foundation (JKFB22-1 to SH), and Kowa Life Science Foundation (to SH). The electron microscopic observations were supported by Research Support Project for Life Science and Drug Discovery (Basis for Supporting Innovative Drug Discovery and Life Science Research (BINDS)) from Japan Agency for Medical Research and Development (AMED) under Grant Number JP23ama121002.

References

1. Hasegawa S, and Inagi R. Organelle stress and crosstalk in kidney disease. *Kidney360.* 2020;1(10):1157-1164.

2. Ge M, et al. The Vicious Cycle of Renal Lipotoxicity and Mitochondrial Dysfunction. *Front Physiol.* 2020;11:732.

3. Tagawa A, et al. Impaired Podocyte Autophagy Exacerbates Proteinuria in Diabetic Nephropathy. *Diabetes.* 2016;65(3):755-767.

4. Hirabayashi Y, et al. ER-mitochondria tethering by PDZD8 regulates Ca(2+) dynamics in mammalian neurons. *Science.* 2017;358(6363):623-630.

5. Nakamura K, et al. Mitochondrial protein FKBP8 captures PDZD8 to form mitochondria-ER contacts. *bioRxiv.* 2023:2023.2008.2022.554218.

6. Shirane M. Lipid Transfer-Dependent Endosome Maturation Mediated by Protrudin and PDZD8 in Neurons. *Front Cell Dev Biol.* 2020;8:615600.

7. Shirane M, et al. Protrudin and PDZD8 contribute to neuronal integrity by promoting lipid extraction required for endosome maturation. *Nat Commun.* 2020;11(1):4576.

8. Elbaz-Alon Y, et al. PDZD8 interacts with Protrudin and Rab7 at ER-late endosome membrane contact sites associated with mitochondria. *Nat Commun.* 2020;11(1):3645.

9. Kleele T, et al. Distinct fission signatures predict mitochondrial degradation or biogenesis. *Nature.* 2021;593(7859):435-439.

10. Guillen-Samander A, et al. PDZD8 mediates a Rab7-dependent interaction of the ER with late endosomes and lysosomes. *Proc Natl Acad Sci U S A.* 2019;116(45):22619-22623.

11. Gao Y, et al. PDZD8-mediated lipid transfer at contacts between the ER and late endosomes/lysosomes is required for neurite outgrowth. *J Cell Sci.* 2022;135(5).

12. Yamamoto T, et al. High-Fat Diet-Induced Lysosomal Dysfunction and Impaired Autophagic Flux Contribute to Lipotoxicity in the Kidney. *J Am Soc Nephrol.* 2017;28(5):1534-1551.

13. Hasegawa S, et al. The oral hypoxia-inducible factor prolyl hydroxylase inhibitor enarodustat counteracts alterations in renal energy metabolism in the early stages of diabetic kidney disease. *Kidney Int.* 2020;97(5):934-950.

14. Hasegawa S, and Inagi R. Harnessing Metabolomics to Describe the Pathophysiology Underlying Progression in Diabetic Kidney Disease. *Curr Diab Rep.* 2021;21(7):21.

15. Fujii R, et al. Decreased IFT88 expression with primary cilia shortening causes mitochondrial dysfunction in cisplatin-induced tubular injury. *Am J Physiol Renal Physiol.* 2021;321(3):F278-F292.

16. Tubbs E, et al. Mitochondria-associated endoplasmic reticulum membrane (MAM) integrity is required for insulin signaling and is implicated in hepatic insulin resistance. *Diabetes.* 2014;63(10):3279-3294.

17. Tubbs E, et al. Disruption of Mitochondria-Associated Endoplasmic Reticulum Membrane (MAM) Integrity Contributes to Muscle Insulin Resistance in Mice and Humans. *Diabetes.* 2018;67(4):636-650.

18. de Brito OM, and Scorrano L. Mitofusin 2 tethers endoplasmic reticulum to mitochondria. *Nature.* 2008;456(7222):605-610.

19. Honrath B, et al. Glucose-regulated protein 75 determines ER-mitochondrial coupling and sensitivity to oxidative stress in neuronal cells. *Cell Death Discov.* 2017;3:17076.

20. Igwebuike C, et al. Cross organelle stress response disruption promotes gentamicin-induced proteotoxicity. *Cell Death Dis.* 2020;11(4):217.

21. Xie Y, et al. Reticulon-1A mediates diabetic kidney disease progression through endoplasmic reticulum-mitochondrial contacts in tubular epithelial cells. *Kidney Int.* 2022;102(2):293-306.

22. Yoshioka K, et al. Lysophosphatidylcholine mediates fast decline in kidney function in diabetic kidney disease. *Kidney Int.* 2021.

23. Sidhom EH, et al. Targeting a Braf/Mapk pathway rescues podocyte lipid peroxidation in CoQ-deficiency kidney disease. *J Clin Invest.* 2021;131(5).

24. Makino SI, et al. Impairment of Proteasome Function in Podocytes Leads to CKD. *J Am Soc Nephrol.* 2021;32(3):597-613.

25. Hartleben B, et al. Autophagy influences glomerular disease susceptibility and maintains podocyte homeostasis in aging mice. *J Clin Invest.* 2010;120(4):1084-1096.

26. Oliva Trejo JA, et al. Transient increase in proteinuria, poly-ubiquitylated proteins and ER stress markers in podocyte-specific autophagy-deficient mice following unilateral nephrectomy. *Biochem Biophys Res Commun.* 2014;446(4):1190-1196.

27. Ducasa GM, et al. ATP-binding cassette A1 deficiency causes cardiolipin-driven mitochondrial dysfunction in podocytes. *J Clin Invest.* 2019;129(8):3387-3400.

28. Grabowski GA, et al. Gaucher disease: Basic and translational science needs for more complete therapy and management. *Mol Genet Metab.* 2021;132(2):59-75.

29. Di Sano F, et al. Glucosylceramide synthase and its functional interaction with RTN-1C regulate chemotherapeutic-induced apoptosis in neuroepithelioma cells. *Cancer Res.* 2003;63(14):3860-3865.

30. Motonishi S, et al. Sirtuin1 Maintains Actin Cytoskeleton by Deacetylation of Cortactin in Injured Podocytes. *J Am Soc Nephrol.* 2015;26(8):1939-1959.

31. O'Hare JK, et al. Compartment-specific tuning of dendritic feature selectivity by intracellular Ca(2+) release. *Science.* 2022;375(6586):eabm1670.

32. Kawashima Y, et al. Single-Shot 10K Proteome Approach: Over 10,000 Protein Identifications by Data-Independent Acquisition-Based Single-Shot Proteomics with Ion Mobility Spectrometry. *J Proteome Res.* 2022;21(6):1418-1427.

33. Kawashima Y, et al. Proteogenomic Analyses of Cellular Lysates Using a Phenol-Guanidinium Thiocyanate Reagent. *J Proteome Res.* 2019;18(1):301-308.

34. Kawashima Y, et al. Optimization of Data-Independent Acquisition Mass Spectrometry for Deep and Highly Sensitive Proteomic Analysis. *Int J Mol Sci.* 2019;20(23).

35. Tyanova S, et al. The Perseus computational platform for comprehensive analysis of (prote)omics data. *Nat Methods.* 2016;13(9):731-740.

36. Zhou Y, et al. Metascape provides a biologist-oriented resource for the analysis of systems-level datasets. *Nat Commun.* 2019;10(1):1523.

37. Nishiumi S, et al. Comparative Evaluation of Plasma Metabolomic Data from Multiple Laboratories. *Metabolites.* 2022;12(2).

38. Takumi H, et al. Comprehensive Analysis of Lipid Composition in Human Foremilk and Hindmilk. *J Oleo Sci.* 2022;71(7):947-957.

39. Yamamoto H, et al. Statistical hypothesis testing of factor loading in principal component analysis and its application to metabolite set enrichment analysis. *BMC Bioinformatics.* 2014;15:51.

40. Livak KJ, and Schmittgen TD. Analysis of relative gene expression data using real-time quantitative PCR and the 2(-Delta Delta C(T)) Method. *Methods.* 2001;25(4):402-408.

41. Mundel P, et al. Rearrangements of the cytoskeleton and cell contacts induce process formation during differentiation of conditionally immortalized mouse podocyte cell lines. *Exp Cell Res.* 1997;236(1):248-258.

42. Shankland SJ, et al. Podocytes in culture: past, present, and future. *Kidney Int.* 2007;72(1):26-36.

43. Schneider CA, et al. NIH Image to ImageJ: 25 years of image analysis. *Nat Methods.* 2012;9(7):671-675.

44. D'Eletto M, et al. Transglutaminase Type 2 Regulates ER-Mitochondria Contact Sites by Interacting with GRP75. *Cell Rep.* 2018;25(13):3573-3581 e3574.

45. Tubbs E, and Rieusset J. Study of Endoplasmic Reticulum and Mitochondria Interactions by In Situ Proximity Ligation Assay in Fixed Cells. *J Vis Exp.* 2016(118).

46. Okuda S, et al. jPOSTrepo: an international standard data repository for proteomes. *Nucleic Acids Res.* 2017;45(D1):D1107-D1111.

Figures and figure legends

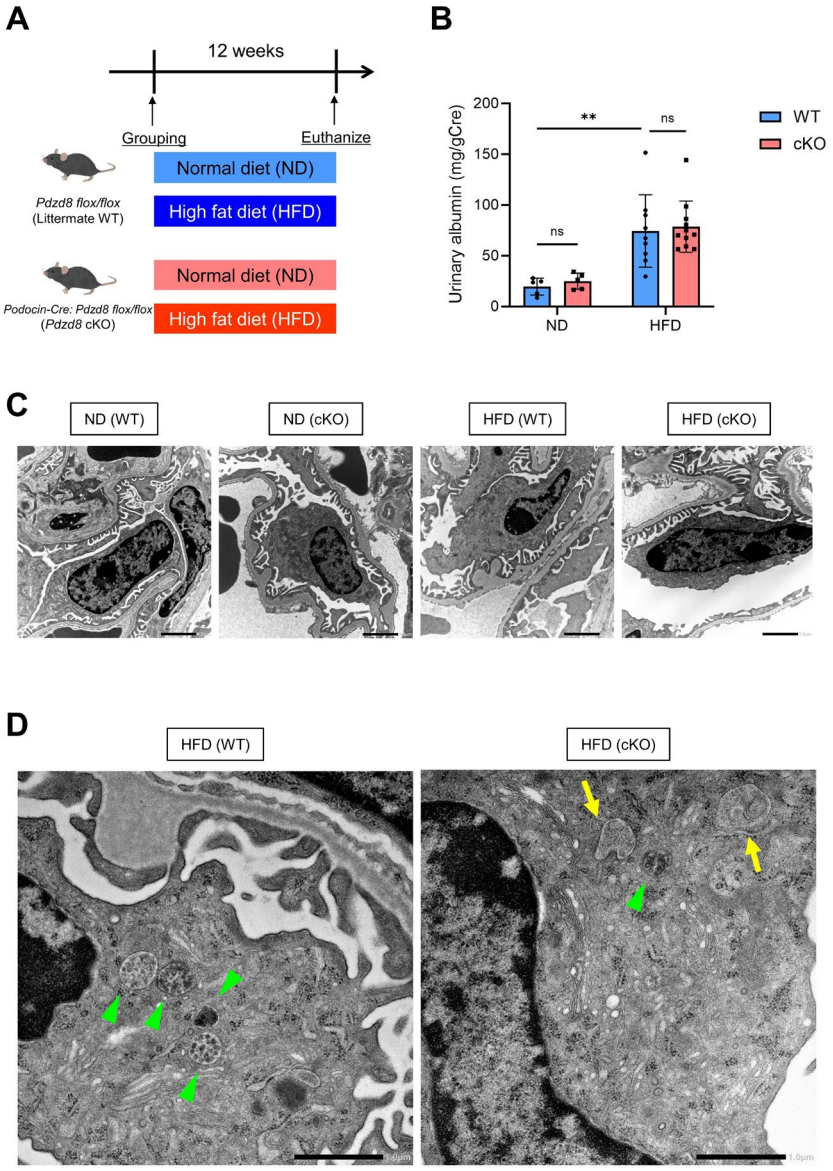

Figure 1. *Pdzd8* deletion induces podocyte endosomal malformation in an obesity-related kidney disease model

(A) The study design is shown (ND: n = 5, HFD: n = 9 or 11). (B) The urinary albumin levels are shown. (C) The electron microscope imaging with low magnification is shown. Scale bar = 2 μm. (D) The electron microscope imaging with high magnification is shown. Scale bar = 1 μm (Green arrowhead: normal endosomes, yellow arrow: abnormal endosomes).

ND, normal diet; HFD, high fat diet; WT, wild-type control mice; cKO, podocyte-specific Pdzd8 knockout mice. Data are presented as mean ± SD. *P*-values are determined by 2-way ANOVA with Tukey's multiple-comparison test. ***P* < 0.01, ns, not significant.

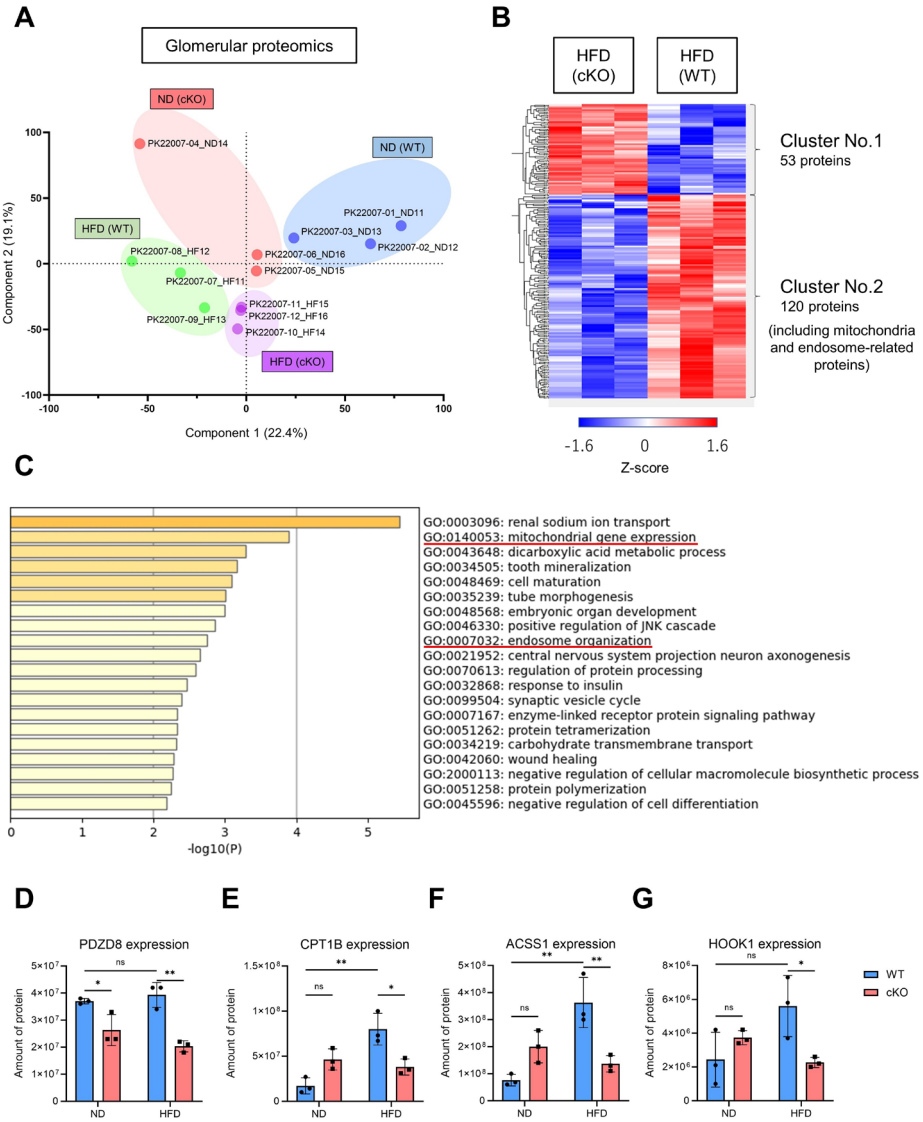

Figure 2. Glomerular proteomics data of an obesity related kidney disease model using podocyte-specific *Pdzd8* knockout mice

(A) Principal component analysis (PCA) plots of the comprehensive proteomics of isolated glomeruli are shown. (B) Heat map of differentially expressed proteins between HFD-WT and HFD cKO groups is shown. (C) Gene ontology analysis of differentially expressed 173 proteins between HFD-WT and HFD-cKO groups is shown. (D) The amount of PDZD8 proteins, (E) carnitine palmitoyltransferase 1b (CPT1B) proteins, (F) acyl-CoA synthetase short chain family member 1 (ACSS1) proteins, (G) hook microtubule tethering protein 1 (HOOK1) proteins are shown (n = 3, each). ND, normal diet; HFD, high fat diet; WT, wild-type control mice; cKO, podocyte-specific *Pdzd8* knockout mice. Data are presented as mean ± SD. *P*-values are determined by 2-way ANOVA with Tukey's multiple-comparison test. **P* < 0.05, ***P* < 0.01, ns, not significant.

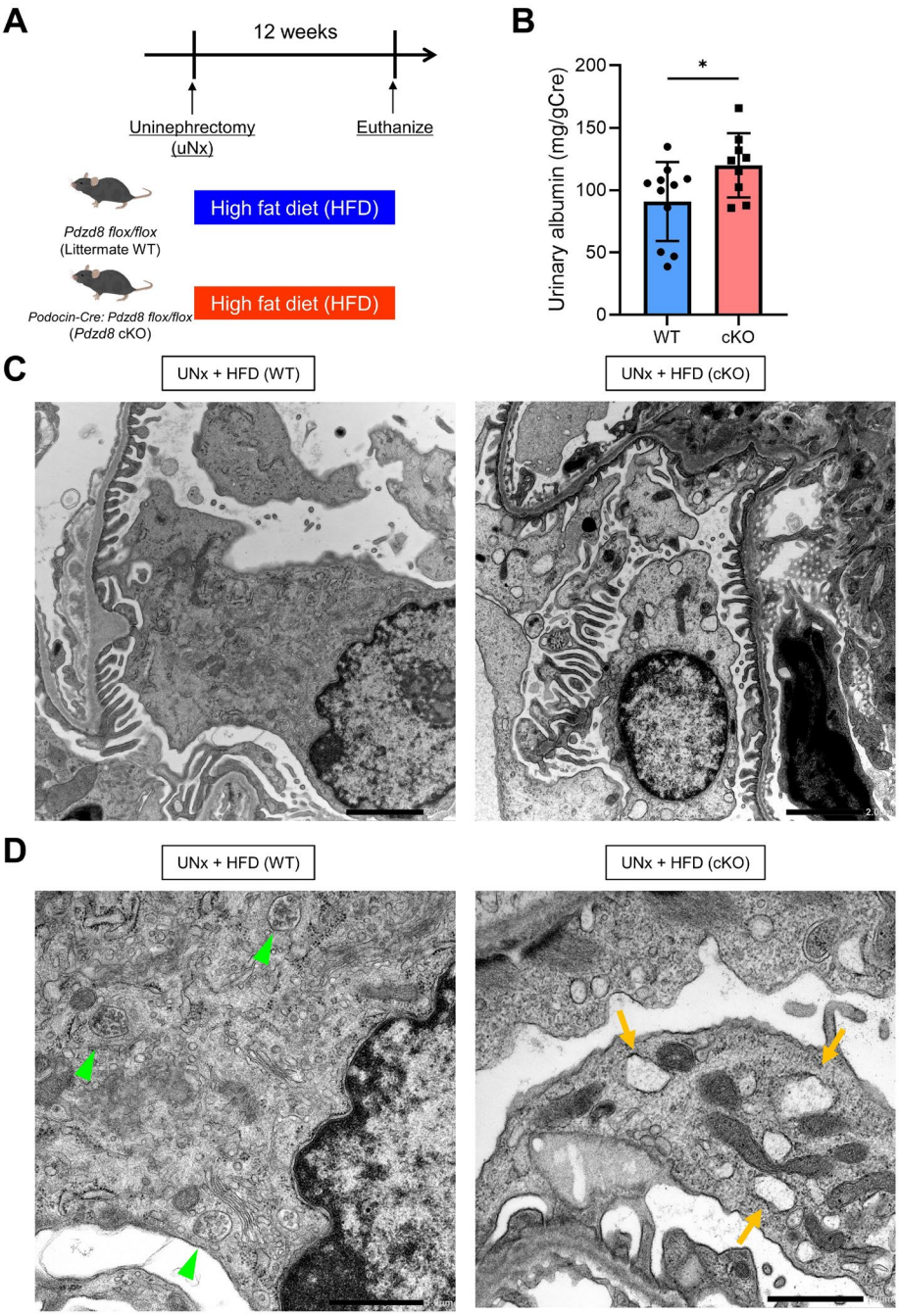

Figure 3. *Pdzd8* deletion leads to the emergence of "fatty endosomes" and exacerbates podocyte injury in an accelerated obesity-related kidney disease model

(A) The study design is shown (n = 9 or 11). (B) The urinary albumin levels are shown. (C) The electron microscope imaging with low magnification is shown. Scale bar = 2 μm. (D) The electron microscope imaging with high magnification is shown. Scale bar = 1 μm (Green arrowhead: normal endosomes, orange arrow: "fatty abnormal endosomes"). Data are presented as mean ± SD. *P*-value is determined by unpaired Student's *t* test. **P* < 0.05.

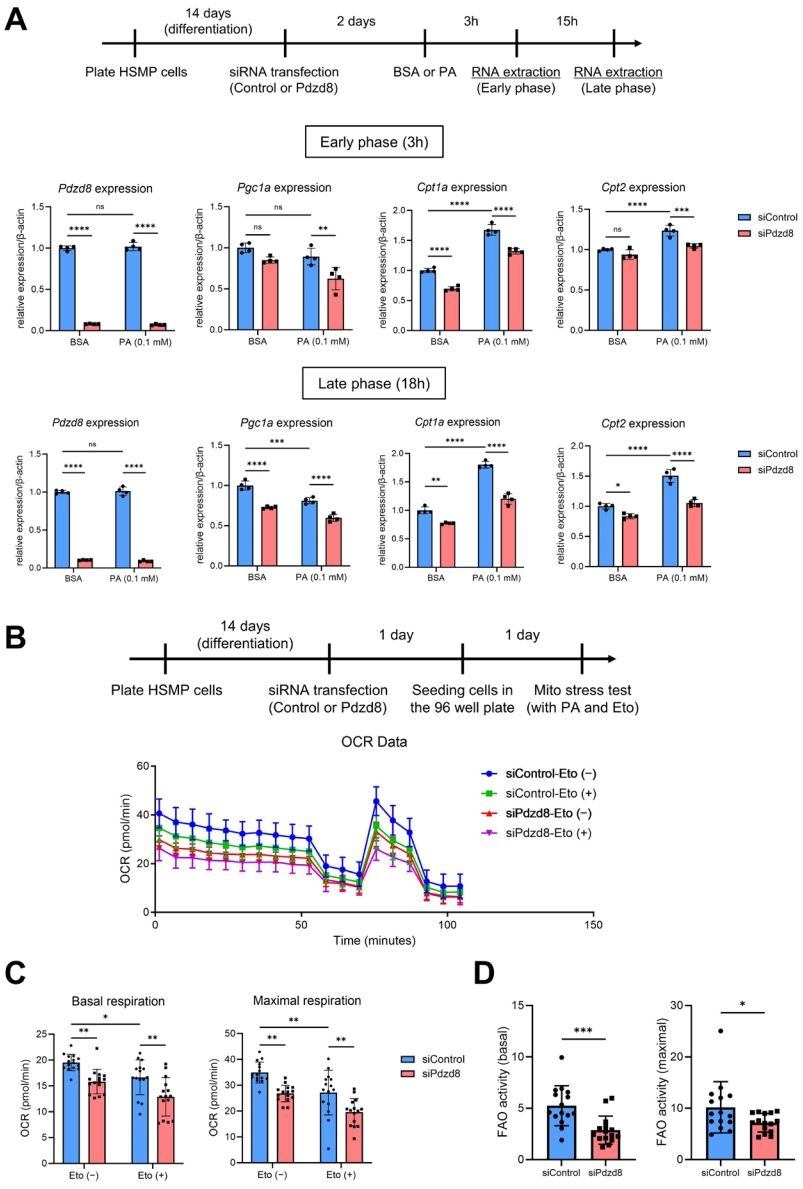

Figure 4. *Pdzd8* knockdown inhibits the activity of mitochondria and fatty acid oxidation (FAO) in podocytes

(A) The results of quantitative real-time PCR are shown (n = 4, each). HSMP, heat sensitive mouse podocytes; BSA, bovine serum albumin; PA, palmitic acids; *Pgc1a*, peroxisome proliferator-activated receptor gamma coactivator 1-alpha; *Cpt1a*, carnitine palmitoyltransferase-1a; *Cpt2*, carnitine palmitoyltransferase-2. (B) (C) (D) The results of Mito stress test are shown (n = 15, each). Eto, etomoxir; OCR, oxygen consumption rate; FAO, fatty acid oxidation.

Data are presented as mean ± SD. *P*-values are determined by 2-way ANOVA with Tukey's multiple-comparison test (A, C) or unpaired Student's *t* test (D). **P* < 0.05, ***P* < 0.01, ****P* < 0.001, *****P* < 0.0001, ns, not significant.

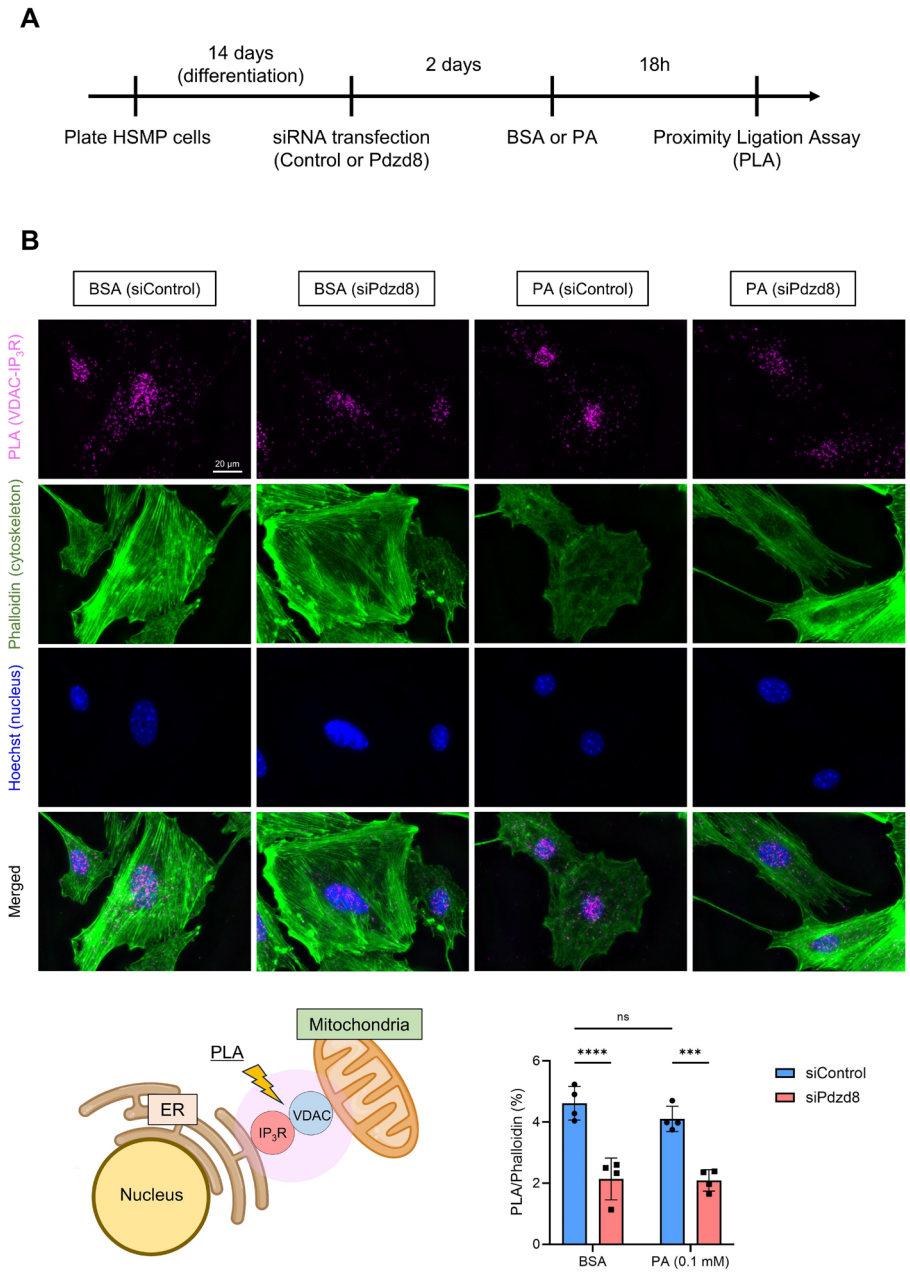

Figure 5. *Pdzd8* knockdown reduces mitochondria-ER contact sites (MERCS) in podocytes

(A) The study design is shown. (B) Proximity ligation between VDAC and IP_3R, phalloidin (cytoskeleton), Hoechst (nucleus) and merged pictures are shown. The process of calculating the ratio of proximity ligation signal to Phalloidin is shown in Supplementary Figure S7 (n = 4, for each). Scale bar = 20 μm.

VDAC, Voltage dependent anion channel; IP_3R, Inositol 1,4,5-trisphosphate receptor. Data are presented as mean ± SD. *P*-values are determined by 2-way ANOVA with Tukey's multiple-comparison test. ***$P < 0.001$, ****$P < 0.0001$, ns, not significant.

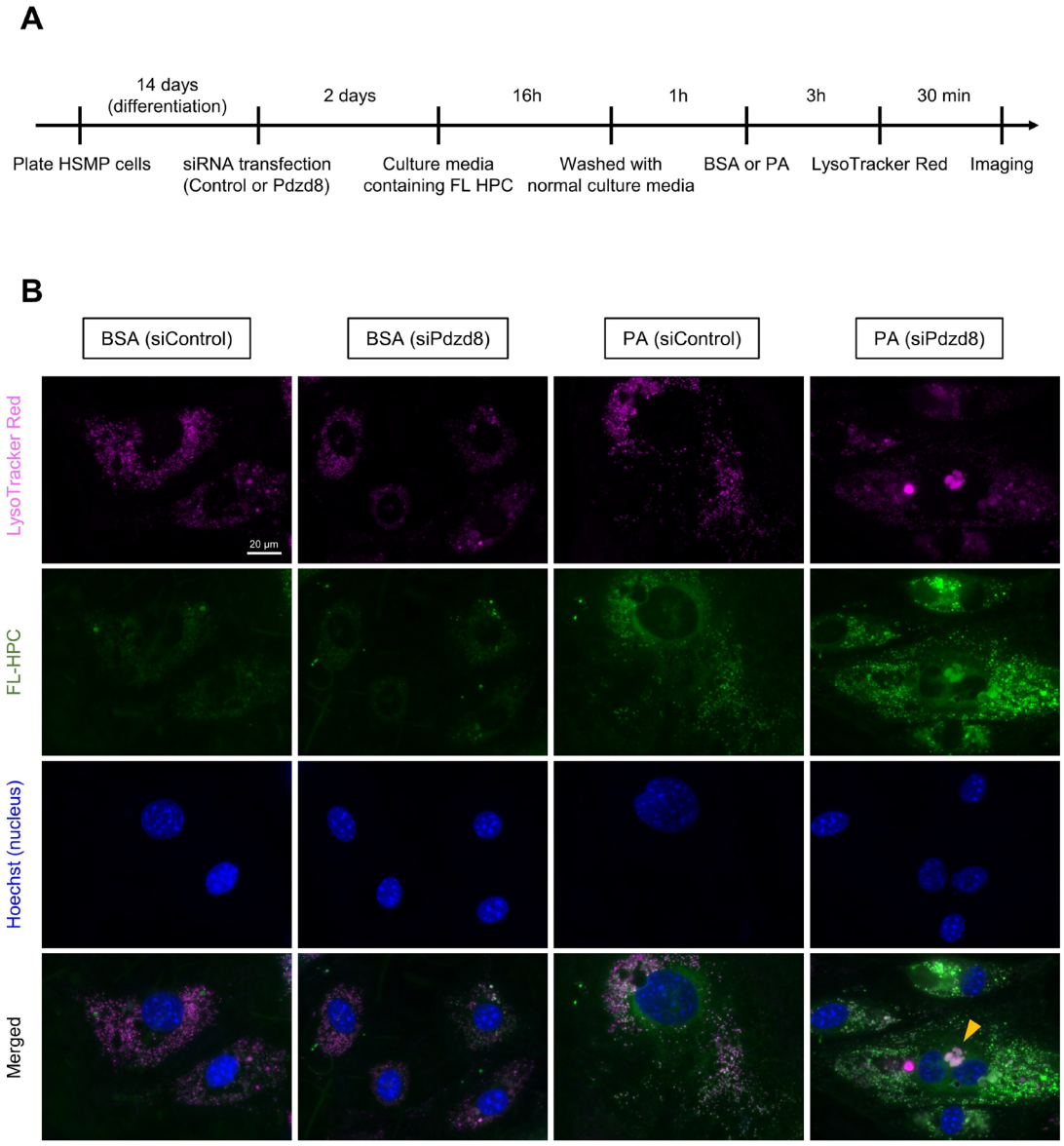

Figure 6. Lipids from cellular membranes accumulate in "fatty endosomes" in *Pdzd8* knockdown podocytes following palmitic acids treatment

(A) The study design is shown.

(B) LysoTracker Red, phosphatidylcholine fluorescence tagged at its fatty acid tail (FL HPC), Hoechst (nucleus), and merged pictures are shown. Scale bar = 20μm (Orange arrowhead: "fatty endosomes").

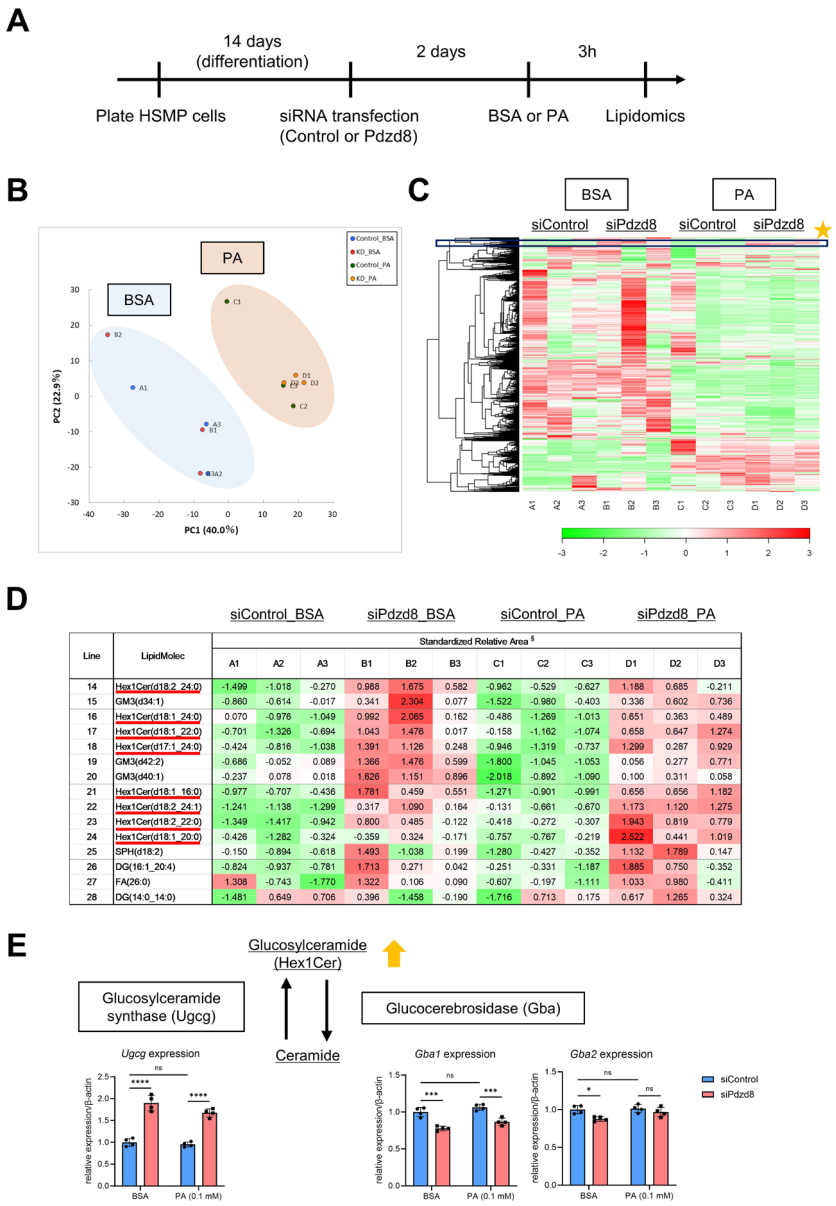

Figure 7. *Pdzd8* knockdown induces the accumulation of glucosylceramide in podocytes

(A) The study design is shown (n = 3, each). (B) Principal component analysis (PCA) plots of the non-targeted lipidomics of cultured podocytes are shown. (C) Heat map of the identified lipids is shown. (D) The excerpt of the lipids that are increased by *Pdzd8* knockdown (the orange star in Figure 7C). (E) The expressions of enzymes for the production and degradation of glucosylceramide are shown (n = 4, each). Hex1cer, glucosylceramide; GM3, gangliosides; SPH, sphingosine; DG, diglyceride; FA, fatty acid; *Ugcg*, UDP-glucose ceramide glucosyltransferase; *Gba1*, glucosylceramidase beta 1; *Gba2*, glucosylceramidase beta 2. Data are presented as mean ± SD. *P*-values are determined by 2-way ANOVA with Tukey's multiple-comparison test. **P* < 0.05, ****P* < 0.001, *****P* < 0.0001, ns, not significant.

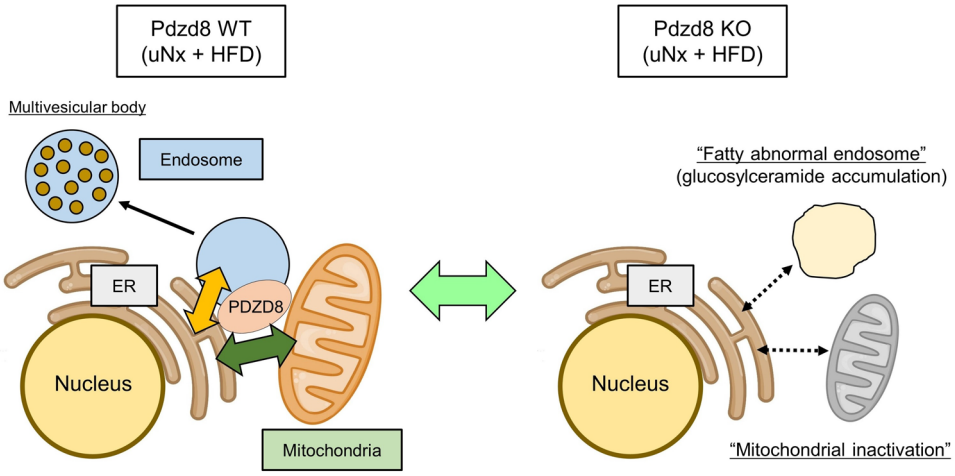

Figure 8. Schemes showing the protective role of organelle communications among ER, mitochondria and endosomes in podocyte lipotoxicity

Our findings demonstrate that PDZD8 serves as a critical organelle-tethering factor, maintaining mitochondrial and endosomal homeostasis during podocyte lipotoxicity.

Tables

Table 1. Primer sequences for the quantitative real-time polymerase chain reactions

Gene name	Forward sequence	Reverse sequence
β-actin (Actb)	AAGATCAAGATCATTGCTCCTCCTG	AAACGCAGCTCAGTAACAGTCC
Pdzd8	TCCATACCAAGCCTTGCAA	CATTTGTTTCTCTGTCATAGGATCC
Cpt1a	GGTCTTCTCGGGTCGAAAGC	TCCTCCCACCAGTCACTCAC
Cpt2	CAATGAGGAAACCCTGAGGA	GATCCTTCATCGGGAAGTCA
Pgc1a	AGTCCCATACACAACCGCAG	CCCTTGGGGTCATTTGGTGA
Ugcg	AGCTGGAGAACTGGTCGCTA	CACACTGTGCGCCATCAG
Gba1	ATGACCAACGCTTGCTGCTA	GTGACTGTACTGCATCCCTC
Gba2	ATCTGCTTGGCTCACGAGTT	TGTCGATGAAAGGGGTCTTC
Itpr3	AAGTACGGCAGCGTGATTCAG	CACGACCACATTATCCCCATTG

Supplementary Materials are provided as separate files.